

# Trajectory tracking control of autonomous heavy-duty mining dump trucks with uncertain dynamic characteristics

Liang CHEN<sup>1</sup>, Zhaobo QIN<sup>1,2</sup>, Manjiang HU<sup>1,2\*</sup>, Hongbo GAO<sup>3\*</sup>, Yougang BIAN<sup>1,2</sup>,  
Biao XU<sup>1,2</sup> & Xiaoyan PENG<sup>1</sup>

<sup>1</sup>State Key Laboratory of Advanced Design and Manufacturing for Vehicle Body, Hunan University, Changsha 410082, China;

<sup>2</sup>Wuxi Intelligent Control Research Institute of Hunan University, Wuxi 214115, China;

<sup>3</sup>Department of Automation, University of Science and Technology of China, Hefei 230026, China

Received 15 September 2022/Revised 11 December 2022/Accepted 16 February 2023/Published online 27 September 2023

**Abstract** The proportion of mines using autonomous mining trucks is still very low at present. To promote the development of intelligent mining, it is urgent to proceed with the drive-by-wire modification to common mining trucks and design a motion control algorithm considering uncertain dynamic characteristics. This paper proposes a trajectory tracking control method for autonomous heavy-duty mining dump trucks (AHMDTs) with uncertain dynamic characteristics. In this method, a driving/braking force compensation algorithm based on an inverse dynamic model is designed to guarantee accurate longitudinal control with less control gain tuning. Using road curvatures, a modified rear-wheel position feedback control method is proposed to deal with reverse-path tracking, which can simultaneously reduce the lateral error and yaw angle error. A modified Stanley controller considering the collaborative preview based on speed and curvature is constructed to achieve accurate path tracking in the forward gear. Moreover, the proposed method focuses on the practice of trajectory tracking control in an open-pit mine condition with the adverse effects caused by uncertain vehicle dynamics, huge variable load, and large actuator lag. Real vehicle tests show that the proposed methodology can control AHMDTs with a low tracking error.

**Keywords** vehicle control, trajectory tracking control, driving/braking force compensation, rear-wheel position feedback

**Citation** Chen L, Qin Z B, Hu M J, et al. Trajectory tracking control of autonomous heavy-duty mining dump trucks with uncertain dynamic characteristics. *Sci China Inf Sci*, 2023, 66(10): 202203, <https://doi.org/10.1007/s11432-022-3713-8>

## 1 Introduction

Since the 21st century, digitization and intelligentization have become important symbols of modern mine construction [1]. In recent years, autonomous heavy-duty mining dump truck (AHMDT) driving technology has gradually emerged in the world and is the key technology of mining engineering equipment automation [2,3]. Komatsu is the first manufacturer to commercialize automatic transportation systems in the mining industry [4]. The automated operation of transportation has been realized [5]. Rio Tinto group [6] operated the first batch of autonomous mining trucks on 1700 km of track, which increased the speed of transporting iron ores by 6% and reduced the impact of changing drivers. Caterpillar has released the Cat MineStar system to realize high efficiency and productivity, extending the tire life and fuel saving [7]. Moreover, Volvo [8] tested an autonomous mining truck inside the earth at a depth of 1320 m. Although some companies have realized the commercialization of autonomous mining trucks, several literature surveys show that there are hardly any research studies that systematically explain how to achieve the trajectory tracking control of AHMDTs in open-pit mines.

Generally, the AHMDT driving system usually includes environmental perception [9,10], motion planning [11,12], and trajectory tracking control [13–15]. Tracking control consists of lateral control and

\* Corresponding author (email: manjiang\_h@hnu.edu.cn, ghb48@ustc.edu.cn)



**Figure 1** (Color online) AHMDT XDE240 and open-pit mines in China.

longitudinal control. Generally, the dynamics-based lateral control is suitable for high-speed conditions. Ni et al. [16] designed a robust lateral controller based on H-infinity and linear matrix inequality approaches, aiming to control autonomous race cars within the limits of a random path. Brown et al. [17] proposed model predictive control based on the nonlinear tire model, and the method finally optimized the front-tire slip angle to reduce the lateral error and ensure lateral stability. However, the dynamic-based control relies on the precise dynamic model, which needs accurate vehicle state and parameter estimation. Generally, the heavy duty and low speed of AHMDTs result in small excitation (e.g., lateral acceleration), and unstructured driving conditions have many strong disturbances in open-pit mines, which are inconvenient for vehicle state and parameter estimation.

In the kinematic-based control method, the model disregards the dynamic components of vehicles. Pure pursuit has been widely used due to the simplicity of implementation, easily tunable parameters, and performance at low velocities [18]. Thrun et al. [19] proposed a Stanley controller that applies the center of the front axle as the reference point to calculate the lateral error and yaw error. Although the kinematic-based control is not suitable for high-speed conditions, existing studies show that the kinematic-based method still has good control accuracy and robustness for medium- and low-speed driving conditions as long as the control parameter or preview distance is set appropriately [20].

Longitudinal control is mainly responsible for tracking the reference speed issued by the planning layer [21]. At present, the longitudinal control architecture is generally segmented into a single layer or double layers [22]. Proportional integral derivative (PID) control is the most common in the engineering field. The Massachusetts Institute of Technology used PID to achieve vehicle longitudinal control in 2007 [23]. As the parameters are relatively fixed, the controller cannot easily adapt to complex conditions. Some researchers applied fuzzy logic control to increase the robustness of PID. Shakouri et al. [24] combined a linear quadratic regulator with PID to control the opening degree of the brake pedal and throttle pedal. To eliminate the influence of noise and parameter uncertainty on the control system, Gerdes et al. [25] adopted the sliding mode controller to calculate the desired acceleration and then realized the tracking of the desired torque by the drive and brake actuators through the lookup table of the inverse dynamic model.

However, most existing studies concentrate on autonomous vehicle driving in urban scenarios. The characteristics of scenarios and vehicles in open-pit mines are quite different, as shown in Figure 1. Specifically, mining dump trucks are heavy (e.g., 110–400 t), and the required traction force is much greater than that of passenger cars, especially when driving uphill slopes of roads. Moreover, there are many climbing and turning road sections in open-pit mines with increased mining depth. Most roads in open-pit mines are rugged, and the terrain conditions of different road sections vary significantly and even abruptly. The proposed trajectory tracking control method focuses on the common heavy-duty mining dump trucks with drive-by-wire modification. Generally, the controller area network (CAN) protocol of most vehicles is not open to the public, which usually leads to the inability to get the important parameters, such as engine torque, motor torque, and brake torque. Hence, it is impossible to establish an accurate longitudinal dynamic model and challengeable to track the reference trajectory under the conditions of huge variable loads and different slopes. In the case of terrible road surface conditions and heavy loads, the trajectory tracking controller should guarantee reasonable accuracy. However, existing trajectory tracking control algorithms do not specifically consider these difficulties faced by AHMDTs and have hardly been implemented on AHMDTs in open-pit mines.

The main contributions of this paper are as follows:



**Figure 2** (Color online) AHMDT platform used in the experiment.

**Table 1** Parameters of the AHMDT

Parameter	Nominal value
Vehicle mass $M_{\text{unload}}$ (kg)	210187
Effective load $M_{\text{load}}$ (kg)	291790
Maximum slope $\theta_{\text{max}}$ (%)	14
Wheelbase $L$ (m)	6.35
Rated power $P$ (kW)	2014
Maximum steering wheel angle $\delta_{\text{max}}$ ( $^{\circ}$ )	31

(1) A driving/braking force compensation (DBFC) algorithm is proposed by considering an inverse dynamic model, which can effectively decrease efforts in tuning longitudinal control gains. Speed tracking and fixed point stopping can be accurately realized under the conditions of heavy loads and large slopes.

(2) A curvature-based rear-wheel position feedback control is proposed to deal with reverse-path tracking, and a modified Stanley controller with a collaborative preview is constructed to achieve forward-path tracking.

(3) The performance of the proposed method is validated with a Komatsu 930E. The experimental results demonstrate that the AHMDT can execute transportation tasks with low tracking errors.

## 2 System modeling

### 2.1 AHMDT platform

An electric AHMDT platform (Komatsu 930E) that applied the proposed trajectory control framework shown in Figure 2 has supported the end-to-end autonomous mining operations, including loading, unloading, and transportation. The AHMDT has realized the by-wire control of the throttle, brake, steering system, and gear shifting system by the drive-by-wire modification. The type of integrated navigation system is CGI-610, as shown in Figure 2, which can achieve a centimeter-level positioning function through real-time kinematics. The parameters of the AHMDT are shown in Table 1.

### 2.2 Actuator test

The drive-by-wire modification of the mining dump truck actuator is very important to realize the autopilot function. The AHMDT is equipped with an electric control steering machine, which can be controlled by the electro-hydraulic proportional control system. In addition, a magnetostrictive sensor is added to the steering cylinder to provide real-time angle signals for steering system control. We obtain the actual value of the steering system by the CAN bus signal. The electric control hydraulic brake system, which can be adjusted by the proportional current, is added to realize the hydraulic brake control of the AHMDT. The percentage of hydraulic brake pressure can be read by the electronic control unit. The

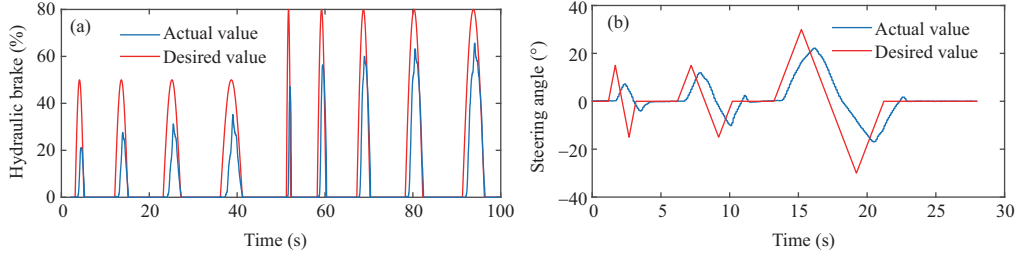


**Figure 3** (Color online) Test results of (a) the hydraulic brake and (b) steering system.

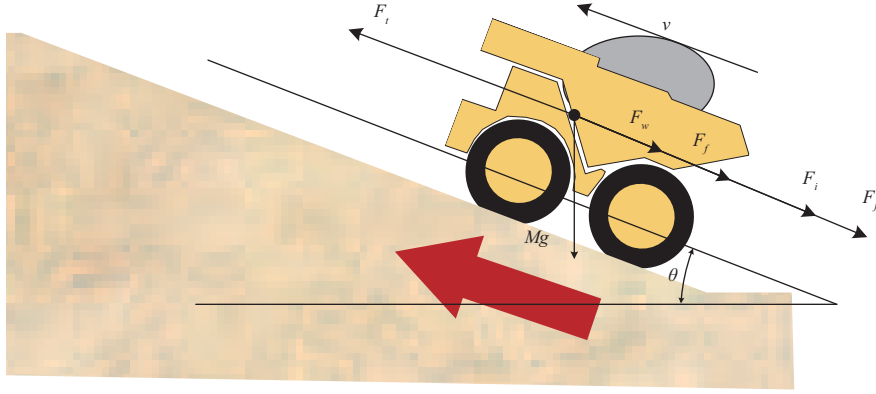


**Figure 4** (Color online) Longitudinal dynamic model of the AHMDT.

paper mainly takes the hydraulic brake and steering system as an example to conduct the actuator test explanation. The hydraulic brake can only be activated below 5 km/h, which is critical to the accuracy of fixed-point parking control.

The results of the triangle wave test for the hydraulic brake system are shown in Figure 3(a). The response lag of the hydraulic brake system is approximately 0.4 s, and the response error is less than 10%. The triangle wave test of the steering system was implemented under a heavy-load condition, as shown in Figure 3(b). Based on the test results, the average response lag of the steering system is approximately 1 s, and the response error is less than 5%. The lag characteristic of the hydraulic actuator is the cause of the big error between the desired value and the actual value. Of note, the hydraulic flow of the steering gear may be slightly insufficient in the heavy-load condition, which will also bring large errors to the actuator test.

### 2.3 Longitudinal model of the AHMDT

In the moving process, the external longitudinal resistances acting on the AHMDT include the aerodynamic resistance  $F_w$ , tire rolling resistance  $F_f$ , climbing resistance  $F_i$ , and acceleration resistance  $F_j$ . The longitudinal dynamic model of AHMDT is shown in Figure 4. These forces and the AHMDT driving force  $F_t$  constitute the force balance in (1):

$$F_t = F_w + F_f + F_i + F_j. \quad (1)$$

Therefore, the longitudinal dynamics can be written as

$$F_t = M\dot{v} + \frac{1}{2}C_D\rho Av^2 + Mgf \cos \theta + Mg \sin \theta, \quad (2)$$

where  $C_D$  is the drag coefficient,  $\rho$  is the air density,  $A$  is the frontal area,  $f$  is the rolling resistance coefficient,  $\theta$  is the road slope,  $M$  is the total mass of the AHMDT,  $g$  is the acceleration due to gravity, and  $\dot{v}$  and  $v$  are the acceleration and current speed of the AHMDT, respectively.

The road-grade estimation is realized by the measured XYZ coordinates and unscented Kalman filter (UKF). The UKF has been widely investigated in the literature, and a summary of the used UKF algorithms is presented in a previous study [26]. The state vector of the UKF is defined as  $X_{Fz} = \theta$ .

$Z_{\text{slope}}$  and  $Z_{\text{slope-p}}$  are the observed vector and predicted vector of the UKF, respectively, which can be calculated as

$$Z_{\text{slope}} = \frac{z}{\sqrt{x^2 + y^2}}, \quad (3)$$

$$Z_{\text{slope-p}} = \tan\theta. \quad (4)$$

In addition, the output power of dynamic operations may slightly deviate from the results of the steady-state operations due to the lag caused by actuators. To mitigate the error, this paper adopts a first-order linear time-invariant system to approach the dynamics:

$$\tau_a \ddot{v} = -\dot{v} + \dot{v}_d, \quad (5)$$

where  $v_d$  is the speed output and  $\tau_a$  is the time constant.

## 2.4 Lateral model of the AHMDT

A precise dynamic model needs accurate vehicle state and parameter estimation (e.g., center of gravity, tire-road friction coefficient, tire cornering stiffness, and tire vertical force). Generally, the heavy duty and low speed of AHMDTs give rise to small excitation (e.g., lateral acceleration), and unstructured driving conditions have many strong disturbances in open-pit mines, which are inconvenient for the vehicle state and parameter estimation. Because the lateral dynamic parameters are difficult to obtain, the study adopts the kinematic model to realize the path-tracking control, which ignores the lateral dynamic factors and is a suitable solution for engineering problems.

It is useful to express the kinematic model with respect to the path in Figure 5. Defining the path as a function of its length  $s$ ,  $\varphi$  and  $\varphi_{\text{des}}$  are the yaw angle of the vehicle and desired vehicle orientation, respectively.  $\delta$  is the steering angle, and  $e_r$  is the orthogonal distance from the center of the rear axle to the path. The yaw angle error of the vehicle with respect to the path is defined as follows:

$$\varphi_e = \varphi_{\text{des}} - \varphi. \quad (6)$$

According to the geometric relation of the kinematic model in path coordinates, differentiating  $\varphi_{\text{des}}$  results in

$$\dot{\varphi}_{\text{des}} = c_r \dot{s}, \quad (7)$$

where  $c_r$  is the curvature of the nearest path point. Differentiating  $\varphi_e$  and  $e_r$  results in

$$\dot{\varphi}_e = \varpi - c_r \dot{s}, \quad (8)$$

$$\dot{e}_r = v_r \sin(\varphi_e), \quad (9)$$

where  $\varpi$  is the yaw rate. Then,  $\dot{s}$  can be defined as

$$\dot{s} = v_r \cos(\varphi_e) + \dot{\varphi}_{\text{des}} e_r. \quad (10)$$

The dynamics of the steering system are difficult to model accurately. To reduce the influence of the actuator lag on the path-tracking control, we used a first-order linear system to approximate the lag of the steering system. On the basis of the steering system test results, the pure lag  $\tau_\delta$  was set to 1 s for the studied platform:

$$\tau_\delta \dot{\delta}_d = -\delta_d + \delta_c, \quad (11)$$

where  $\delta_c$  is the steering angle command and  $\delta_d$  is the desired steering angle.

Substituting  $(s, e_r, \varphi_e)$  and the kinematic bicycle model in (9), the kinematic model in the path coordinates can be defined as follows:

$$\begin{bmatrix} \dot{s} \\ \dot{e}_r \\ \dot{\varphi}_e \\ \dot{\delta}_d \end{bmatrix} = \begin{bmatrix} \frac{\cos(\varphi_e)}{1-c_r e_r} & 0 \\ \sin(\varphi_e) & 0 \\ \frac{\tan(\delta)}{L} + \frac{c_r v_r \cos(\varphi_e)}{1-c_r e_r} & 0 \\ 0 & -\frac{1}{\tau_\delta} \end{bmatrix} \begin{bmatrix} v \\ \delta_d \end{bmatrix} + \begin{bmatrix} 0 \\ 0 \\ 0 \\ \frac{1}{\tau_\delta} \end{bmatrix} \delta_c. \quad (12)$$

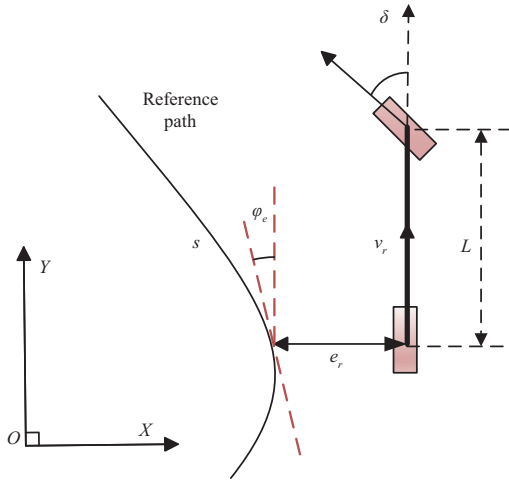


**Figure 5** (Color online) Kinematic model in path coordinates.

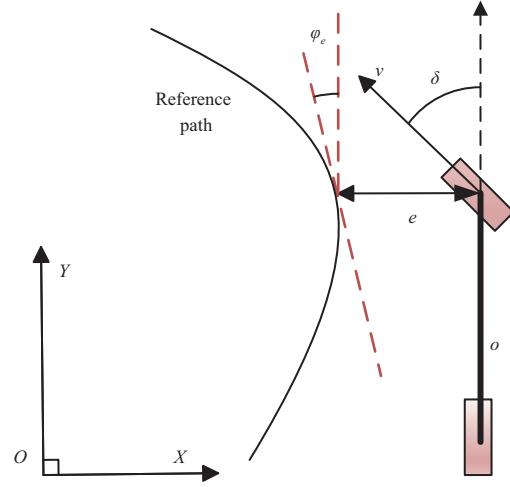


**Figure 6** (Color online) Geometric model of the Stanley controller.

In addition, the Stanley control is a popular path-tracking approach. The control model needs the lateral error and yaw angle error calculated by the nearest path point and the center of the front axle. The geometric model is shown in Figure 6. According to the geometric relationship, the lateral error rate can be calculated as follows:

$$\dot{e} = v_f \sin(\varphi_e + \delta), \quad (13)$$

where  $e$  is the lateral error between the nearest path point and the center of the front axle and  $v_f$  is the longitudinal speed.

The lateral error rate in (13) is directly determined by the front-wheel steering angle, which can be solved by setting  $\dot{e} = ke$  to realize the error convergence.

$$\delta = \arctan\left(\frac{-ke}{v_f}\right) - \varphi_e, \quad (14)$$

where  $k$  is the controller gain [22]. The steering angle command  $\delta_d$  can be determined by (10).

The internal parameters of the lateral model can be divided into three categories, namely, motion information, reference trajectory information, and vehicle parameter. Motion information can be measured by the integrated differential global position system (DGPS) and inertial measurement unit (IMU). The reference trajectory information can be generated by path planning. The vehicle parameters, such as the wheelbase, can be measured by hand.

### 3 Trajectory tracking control framework

The overall system block diagram of the proposed trajectory control method is shown in Figure 7. It consists of five control models: slope-start control model, speed tracking model, fixed-point parking model, forward lateral control model, and reverse lateral control model. When the AHMDT is far from the destination, the speed tracking mode is activated in the longitudinal controller. After determining the drive/brake model based on the corrected speed error, the proposed DBFC algorithm and speed feedback control (SFC) are used to achieve accurate longitudinal control of the AHMDT. The lateral controller is divided into the forward control mode and the reverse control mode. Of note, road curvature should be distinguished between positive and negative in the modified rear-wheel position feedback controller (MRFC).

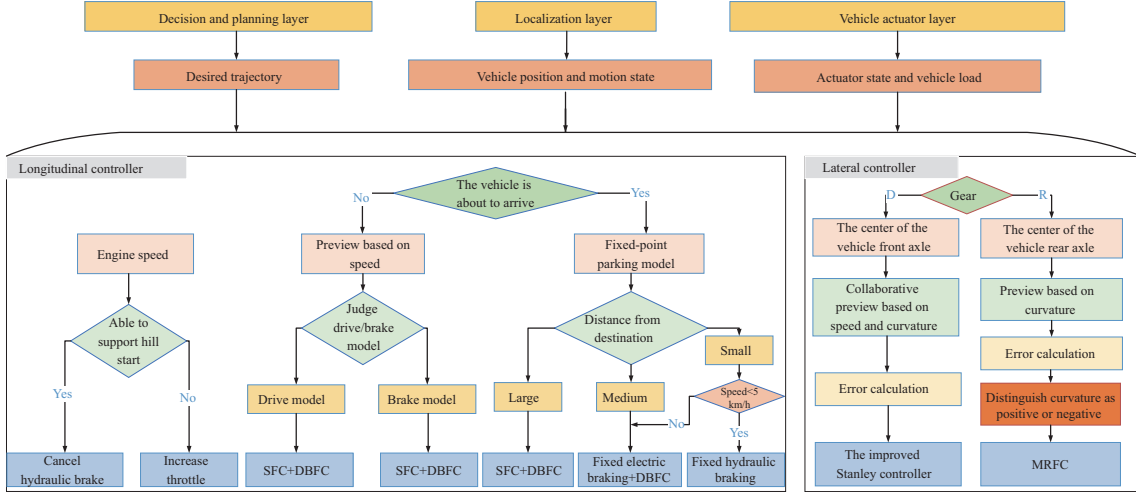


Figure 7 (Color online) Overall system block diagram.

## 4 Longitudinal controller design

### 4.1 DBFC

Because the longitudinal dynamic characteristics of AHMDTs are uncertain, this study applied SFC to achieve longitudinal control. However, the difference in the AHMDT total mass between a heavy load and a light load is huge, and the road slope in open-pit mines is changeable. A longitudinal controller requires different gains to constitute several PID strategies, which is cumbersome for tuning control parameters. This study also integrated the DBFC and SFC to overcome the problem. The logical diagram of the speed tracking model is shown in Figure 8. The main idea is to apply SFC to achieve longitudinal control under the no-load and flat conditions using a set of SFC parameters. For different loads and slopes, the DBFC strategy is applied to realize the compensation of brake and throttle, and the inverse dynamic model and actuator lag model are used to model the uncertain dynamics without the need for vehicle engine torque, motor torque, and brake torque signals.

First, by analyzing the inverse dynamic model, the driving/braking force of the unloaded AHMDT on the flat road,  $F_{\text{normal}}$ , can be first calculated:

$$F_{\text{normal}} = M_{\text{unload}}(a_{\text{des}} + gf) + \frac{1}{2}C_D\rho Av^2, \quad (15)$$

where  $M_{\text{unload}}$  is the unloading mass of the AHMDT and  $a_{\text{des}}$  is the desired longitudinal acceleration, which can be calculated with the desired speed  $v_{\text{des}}$  and current speed  $v_d$ :

$$a_{\text{des}} = k_d \left( v_{\text{des}} - \int_0^{\Delta t} (\tau_a \ddot{v} + \dot{v}) dt \right), \quad (16)$$

where  $k_d$  is the proportional coefficient.

Then, the driving/braking force under the current state of the AHMDT,  $F_{\text{desire}}$ , is calculated:

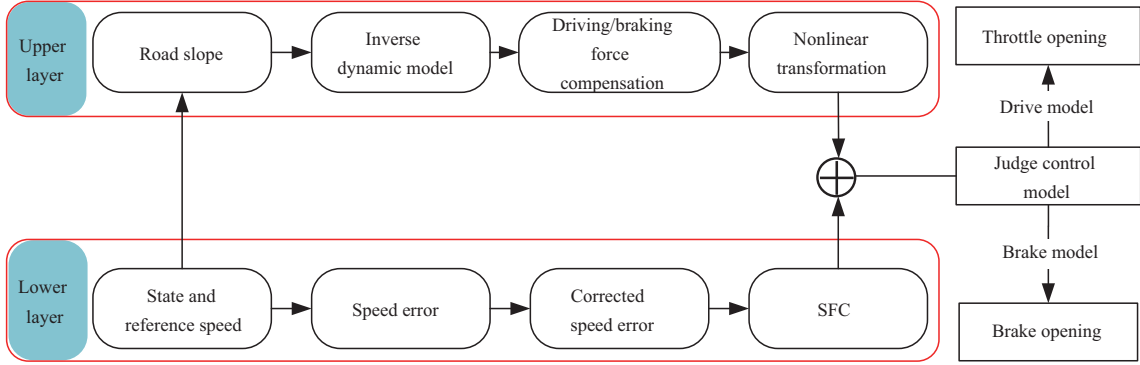
$$F_{\text{desire}} = M(a_{\text{des}} + gf \cos \theta + g \sin \theta) + \frac{1}{2}C_D\rho Av^2. \quad (17)$$

The influence of the rampway relative to the flat road on the driving/braking force needed by the AHMDT can be obtained:

$$F_e = F_{\text{desire}} - F_{\text{normal}}, \quad (18)$$

where  $F_e$  is the driving/braking force deviation (DBFD).

After obtaining the DBFD under different slope and load conditions, the uphill and downhill corresponding relationship between the DBFD and the compensation of the throttle/brake is calibrated by manual experience. The calibrated results are shown in Tables 2 and 3. Because the mine transport standard specifies the range of the road slope, speed, maximum acceleration, and load of the vehicle,


**Figure 8** (Color online) Logical diagram of the speed tracking model.

**Table 2** Calibrated results for the uphill condition

	$F_{eu1}$	$F_{eu2}$	$F_{eu3}$	$F_{eu4}$	$F_{eu5}$
$\alpha_{c\_uphill}$	$\alpha_{cu1}$	$\alpha_{cu2}$	$\alpha_{cu3}$	$\alpha_{cu4}$	$\alpha_{cu5}$
$p_{c\_uphill}$	$p_{cu1}$	$p_{cu2}$	$p_{cu3}$	$p_{cu4}$	$p_{cu5}$

**Table 3** Calibrated results for the downhill condition

	$F_{ed1}$	$F_{ed2}$	$F_{ed3}$	$F_{ed4}$	$F_{ed5}$
$\alpha_{c\_downhill}$	$\alpha_{cd1}$	$\alpha_{cd2}$	$\alpha_{cd3}$	$\alpha_{cd4}$	$\alpha_{cd5}$
$p_{c\_downhill}$	$p_{cd1}$	$p_{cd2}$	$p_{cd3}$	$p_{cd4}$	$p_{cd5}$

the upper and lower bounds of the DBFD, which are  $F_{eu1}$ ,  $F_{eu5}$ ,  $F_{ed1}$ , and  $F_{ed5}$ , can be calculated for all possible conditions. In the range of the DBFD, the  $N$  groups of the DBFD are selected by a fixed proportion  $\varsigma$ .  $N$  is a positive integer, which can be set as required. In this paper, five groups of DBFDs are expressed as an example.  $F_{e\_uphill}$  and  $F_{e\_downhill}$  are the uphill and downhill DBFD, respectively.  $\alpha_{c\_uphill}$ ,  $p_{c\_uphill}$ ,  $\alpha_{c\_downhill}$ , and  $p_{c\_downhill}$  are the calibrated compensation of the throttle and brake.  $\alpha_{cui}$ ,  $p_{cui}$ ,  $\alpha_{cdi}$ , and  $p_{cdi}$  are the specific calibration values, and  $i = \{1, 2, 3, 4, 5\}$  is the index of calibrated data.

Then, the proportional coefficient calculated by the current DBFD and the range of the DBFD can be described:

$$\Gamma_u = \frac{|F_e - F_{eu1}|}{\varsigma}, \quad (19)$$

$$\Gamma_d = \frac{|F_e - F_{ed1}|}{\varsigma}, \quad (20)$$

where  $\Gamma_u$  and  $\Gamma_d$  represent the proportional coefficients going uphill and downhill, respectively.

Finally, the current compensation of the throttle and brake when going uphill can be concluded:

$$\alpha_{cu} = \alpha_{cui} + (\alpha_{cu(i+1)} - \alpha_{cui})(\Gamma_u - i), \quad i = \lfloor \Gamma_u \rfloor, \quad (21)$$

$$p_{cu} = p_{cui} + (p_{cu(i+1)} - p_{cui})(\Gamma_u - i), \quad i = \lfloor \Gamma_u \rfloor, \quad (22)$$

where  $\lfloor \cdot \rfloor$  indicates that the value is rounded down.  $\alpha_{cu}$  is the current compensation of the throttle going uphill, and  $p_{cu}$  is the current compensation of the brake going uphill.  $i + 1$  means that the index of the calibrated value is increased by 1.

The current compensation of the throttle and brake going downhill can be concluded:

$$\alpha_{cd} = \alpha_{cdi} + (\alpha_{cd(i+1)} - \alpha_{cdi})(\Gamma_d - i), \quad i = \lfloor \Gamma_d \rfloor, \quad (23)$$

$$p_{cd} = p_{cdi} + (p_{cd(i+1)} - p_{cdi})(\Gamma_d - i), \quad i = \lfloor \Gamma_d \rfloor, \quad (24)$$

where  $\alpha_{cd}$  is the current compensation of the throttle going downhill and  $p_{cd}$  is the current compensation of the brake going downhill. In this way, we can model the uncertain dynamics and realize the longitudinal control under the condition of a huge variable load and different slopes.

## 4.2 SFC

The first step is to find a trajectory point nearest to the center of the vehicle rear axle. Because the two trajectories may coincide, but in opposite directions, the heading angle of the trajectory point needs to be compared with the current yaw angle of the vehicle. The angle constraint can be described as follows:

$$|\varphi_{\text{des}} - \varphi| < \frac{1}{2}\pi \quad \text{or} \quad |\varphi_{\text{des}} - \varphi| > \frac{3}{2}\pi. \quad (25)$$

Then, the DBFC can be used to correct the speed error:

$$v_{\text{revise}} = v - v_{\text{des}} - k_e F_e, \quad (26)$$

where  $k_e$  is the dimensionless proportional coefficient and  $v_{\text{revise}}$  is the corrected speed error.

To guarantee the speed tracking accuracy under acceleration and deceleration switching, the switching logic of the speed tracking mode should be designed, and the dead-zone bias  $\vartheta$  should be set for the corrected speed error. The switching logic is formulated as follows:

$$\text{Ctrl} = \begin{cases} \text{driving\_ctrl}, & v_{\text{revise}} > \vartheta, \\ \text{remain\_unchanged}, & -\vartheta < v_{\text{revise}} \leq \vartheta, \\ \text{braking\_ctrl}, & v_{\text{revise}} \leq -\vartheta, \end{cases} \quad (27)$$

where Ctrl is the speed tracking model; driving\_ctrl and braking\_ctrl are the drive mode and brake mode, respectively; and remain\_unchanged represents that the system maintains the current Ctrl.

The current compensation of the throttle and brake can be calculated by the DBFC strategy.

$$\text{Control\_c} = \begin{cases} \alpha_{\text{cu}}, & \theta > 0 \ \& \ \text{Ctrl} = \text{driving\_ctrl}, \\ p_{\text{cu}}, & \theta \leq 0 \ \& \ \text{Ctrl} = \text{driving\_ctrl}, \\ \alpha_{\text{cd}}, & \theta > 0 \ \& \ \text{Ctrl} = \text{braking\_ctrl}, \\ p_{\text{cd}}, & \theta \leq 0 \ \& \ \text{Ctrl} = \text{braking\_ctrl}. \end{cases} \quad (28)$$

If the next moment is the drive mode, the SFC based on the DBFC law can be concluded as

$$\alpha_d = \text{Control\_c} + k_{p-\alpha}(v - v_{\text{des}}) + k_{i-\alpha} \int_0^{\Delta t} (v - v_{\text{des}}) dt, \quad (29)$$

where  $\alpha_d$  is the desired throttle opening;  $k_{p-\alpha}$  and  $k_{i-\alpha}$  are the proportional coefficient and integral coefficient, respectively;  $\Delta t$  is the sampling time of the system.

If the next moment is the brake mode, the SFC based on the DBFC law can be concluded as

$$p_d = \text{Control\_c} + k_{p-p}(v - v_{\text{des}}) + k_{i-p} \int_0^{\Delta t} (v - v_{\text{des}}) dt, \quad (30)$$

where  $p_d$  is the desired brake opening and  $k_{p-p}$  and  $k_{i-p}$  are the proportional coefficient and integral coefficient, respectively.

There is only one set of SFC parameters, which may lead to overshoot, such as rapid acceleration or deceleration for AHMDTs. However, if the proportional coefficient is diminished, the speed error may converge too slowly. A trade-off exists between the speed of the error convergence and the reduction of overshooting. To figure out the problem, the adaptive tuning method of the integral coefficient is designed by the proportional and integral of (29) and (30), which can make the error converge quickly and reduce the speed overshoot as far as possible. Specific strategies can be described as follows:

$$k_i = \begin{cases} 0, & (v - v_{\text{des}}) > 0 \ \& \ \int_0^{\Delta t} (v - v_{\text{des}}) dt \leq 0, \\ \tau_1, & (v - v_{\text{des}}) > 0 \ \& \ \int_0^{\Delta t} (v - v_{\text{des}}) dt > 0, \\ 0, & (v - v_{\text{des}}) \leq 0 \ \& \ \int_0^{\Delta t} (v - v_{\text{des}}) dt > 0, \\ \tau_2, & (v - v_{\text{des}}) \leq 0 \ \& \ \int_0^{\Delta t} (v - v_{\text{des}}) dt \leq 0, \end{cases} \quad (31)$$

where  $k_i$  is the integral coefficient in SFC, and  $\tau_1$  and  $\tau_2$  are the positive constants.

**Remark 1.** Generally, integral feedback guarantees the complete elimination of steady-state errors. The drawback, however, is that because of its responsiveness to past errors, a high gain can result in large overshoot and poor overall transient response [27]. By tuning the integral coefficient of the longitudinal controller, we found that the integral feedback does not always promote the convergence of speed tracking errors when the drive mode and brake mode are switched. If the AHMDT suddenly needs to achieve a large acceleration, the speed tracking error will slowly converge due to the negative effect of the integral feedback. Therefore, we designed an adaptive adjustment strategy shown in (31) according to the positive and negative values of the proportional and integral coefficients of (29) and (30) to solve the above problems. The integral feedback with a negative effect will be set to zero, which is suitable for the drive mode and brake mode.

### 4.3 Fixed-point parking control

For fixed-point parking control with large distances, the vehicle control layer no longer receives the desired speed issued by the planning layer. The fixed-point parking mode performs the SFC and DBFC algorithms through the desired speed set in advance to reduce the speed to a certain range as soon as possible. For fixed-point parking control with a medium distance, different electrical brake values and the DBFC algorithm are used for segmented control. Finally, when the AHMDT enters a small distance range and the speed is below 5 km/h, different fixed hydraulic brake values are adopted to realize the accurate fixed-point parking of the AHMDT.

### 4.4 Slope-start control

For the slope-start control model, the engine speed should be evaluated first. If the current engine speed can support the vehicle to start on the slope, the hydraulic brake can be released. Otherwise, the system continues to increase the throttle opening to adjust the engine speed to achieve slope-start control for the AHMDT.

## 5 Lateral controller design

### 5.1 Modified rear-wheel position feedback controller

For reverse lateral control, after calculating the lateral error and yaw angle error by the preview path point, a modified rear-wheel position feedback controller is proposed. The preview path point is selected by taking the center of the rear axle as the reference point and considering the influence of the path curvature. In addition, the road curvature should be distinguished between positive and negative in the application. Similarly, after the nearest path point is determined by (25), the preview path point can be selected to realize the reverse lateral control based on the preview.

According to the kinematic model in path coordinates, the yaw angle error rate  $\dot{\varphi}_e$  provides a local asymptotic convergence to two continuously differentiable paths:

$$\omega = \frac{c_r v_r \cos(\varphi_e)}{1 - c_r e_r} - g_1(e_r, \varphi_e) \varphi_e - k_e v_r \frac{\sin(\varphi_e)}{\varphi_e} e_r, \quad (32)$$

where  $g_1(e_r, \varphi_e)$  and  $k_e$  are positive constants and  $v_r$  is not equal to 0, which has been proven in [28] by the Lyapunov function  $V(\varphi_e, e_r) = e_r^2 + \varphi_e^2/\gamma$  using the coordinate system. Setting  $g_1(e_r, \varphi_e) = k_\varphi |v_r|$  for  $k_e > 0$  leads to a local exponential convergence with a rate independent of the vehicle speed until  $v_r \neq 0$ . The yaw rate of the vehicle is designed as follows:

$$\omega = \frac{c_r v_r \cos(\varphi_e)}{1 - c_r e_r} - (k_\varphi |v_r|) \varphi_e - k_e v_r \frac{\sin(\varphi_e)}{\varphi_e} e_r. \quad (33)$$

Because the prescribed reverse speed of the AHMDT is usually less than 10 km/h, the preview point is selected only according to the path curvature under the common reversal scene in open-pit mines. The preview distance  $d_{pr}$  can be selected dynamically:

$$d_{pr} = \begin{cases} d_{hr}, & c_r > 0.1, \\ d_{mr}, & 0.05 \leq c_r \leq 0.1, \\ d_{lr}, & c_r < 0.05, \end{cases} \quad (34)$$

where  $d_{hr}$ ,  $d_{mr}$ , and  $d_{lr}$  are the preview distances calibrated by the different curvature ranges.

Then, the distance traversal is applied to determine the preview path point. The yaw angle error is calculated in (6), and the lateral error  $e_{pr}$  can be concluded:

$$e_{pr} = (x_r - x_{pr}) \sin(\varphi_p) - (y_r - y_{pr}) \cos(\varphi_p), \quad (35)$$

where  $x_r$  and  $y_r$  are the coordinates of the rear axle center and  $x_{pr}$  and  $y_{pr}$  are the coordinates of the preview path point selected by the rear axle center.

In light of the Ackermann steering theorem and (12), the desired steering angle and its derivative can be described:

$$\delta_d = \arctan \left\{ L \left( \frac{c_r \cos(\varphi_e)}{1 - c_r e_r} - k_\varphi \varphi_e - k_e e_r \right) \right\}, \quad (36)$$

$$\dot{\delta}_d = \frac{\dot{c}_r \cos(\varphi_e) - c_r \dot{\varphi}_e \sin(\varphi_e) - c_r^2 (-e_r \dot{\varphi}_e \sin(\varphi_e) - \dot{e}_r \cos(\varphi_e))}{(1 - c_r e_r)^2 + (L c_r \cos(\varphi_e) - L(1 - c_r e_r)(k_\varphi \varphi_e - k_e e_r))^2}, \quad (37)$$

where  $L$  is the AHMDT wheelbase. Eq. (37) can be further simplified by the geometric relation in Figure 6 and small-angle approximation for  $\varphi_e$ :

$$\dot{\delta}_d = \frac{(\dot{c}_r + c_r^2 v_r \varphi_e) \cos \varphi_e - (c_r - c_r^2 e_r)(\varpi - c_r v_r) \varphi_e}{(1 - c_r e_r)^2 + L^2 (c_r - (1 - c_r e_r)(k_\varphi \varphi_e - k_e e_r))^2}. \quad (38)$$

The final control law of the MRFC can be described as follows:

$$\begin{aligned} \delta_c = & \arctan \left\{ L \left( \frac{c_r \cos(\varphi_e)}{1 - c_r e_r} - k_\varphi \varphi_e - k_e e_r \right) \right\} \\ & + \int_0^{\Delta t} \frac{\tau_\delta (\dot{c}_r + c_r^2 v_r \varphi_e) \cos \varphi_e - \tau_\delta (c_r - c_r^2 e_r)(\varpi - c_r v_r) \varphi_e}{(1 - c_r e_r)^2 + L^2 (c_r - (1 - c_r e_r)(k_\varphi \varphi_e - k_e e_r))^2} dt. \end{aligned} \quad (39)$$

**Remark 2.** (a) The road curvature  $c_r$  should be distinguished as positive or negative. (b) The small-angle approximation,  $\sin(\varphi_e) \approx \varphi_e$ , is applied to avoid the disturbance caused by the change of the yaw angle error. (c) The MRFC is only for reverse gear, so the positive and negative effects of speed can be ignored, and the speed can be approximated and simplified in the denominator. (d) The procedure for determining the control gains has been derived in [28]. The two gains can be described as  $k_\varphi = 2\zeta a$  and  $k_e = a^2$ .  $\zeta$  is the damping factor, which can suppress overshoot, and  $a$  is the positive constant that can make the errors converge.

## 5.2 Modified Stanley controller

To achieve steering control when the vehicle is in the forward gear, a modified Stanley controller considering collaborative preview based on speed and curvature is constructed. According to the current speed feedback and the curvature of the nearest path point, the preview distance can be selected dynamically after the nearest path point is determined in (25):

$$d_{pv} = k_{pv} v \Delta t, \quad (40)$$

$$d_{pc} = \begin{cases} d_{hc}, & c_r > 0.05, \\ d_{mc}, & 0.05 \leq c_r \leq 0.05, \\ d_{lc}, & c_r < 0.05. \end{cases} \quad (41)$$

The final preview distance can be expressed as  $d_p = \max\{d_{pv}, d_{pc}\}$ .  $d_{pv}$  and  $d_{pc}$  are the preview distances determined according to the speed feedback and the curvature of the nearest path point, and  $k_{pv}$  is the proportionality coefficient.  $d_{hc}$ ,  $d_{mc}$ , and  $d_{lc}$  are the preview distance calibrated by different curvature ranges, and  $c_r$  is the curvature of the nearest path point.

The yaw angle error between the preview point and the center of the front axle  $\varphi_{ep}$  can be expressed as follows:

$$\varphi_{ep} = \varphi - \varphi_p, \quad (42)$$

where  $\varphi$  and  $\varphi_p$  are the yaw angle of the vehicle and desired vehicle orientation determined by the preview path point, respectively. The lateral error  $e_p$  can be concluded as

$$e_p = (x_0 - x_p) \sin(\varphi_p) - (y_0 - y_p) \cos(\varphi_p), \quad (43)$$

where  $x_0$  and  $y_0$  are the coordinates of the front axle center, and  $x_p$  and  $y_p$  are the coordinates of the preview path point. Then, the desired steering angle and its derivative can be described as

$$\delta_d = \arctan\left(\frac{-ke_p}{v_f}\right) - \varphi_{ep}, \quad (44)$$

$$\dot{\delta}_d = \frac{kv_f^2(e_p\dot{v}_f - v_f\dot{e}_p)}{v_f^2 + (ke_p)^2} - \dot{\varphi}_{ep}. \quad (45)$$

The modified Stanley controller is designed by the geometric relation (6) and (11):

$$\delta_c = \arctan\left(\frac{-ke_p}{v_f}\right) - \varphi_{ep} + \int_0^{\Delta t} \left[ \frac{kv_f^2(e_p\dot{v}_f - v_f^2(\varphi_{ep} + \delta))}{v_f^2 + (ke_p)^2} - c_{rp}v_f \right] dt. \quad (46)$$

Moreover, to guarantee path-tracking accuracy, the control gain is adjusted adaptively based on the curvature of the preview path point and the lateral error:

$$k = \begin{cases} \kappa_1 c_{rp}, & 0 < |c_{rp}| \leq 0.02, \\ \kappa_1 c_{rp} + \kappa_2 e_p, & |c_{rp}| > 0.02, \end{cases} \quad (47)$$

where  $c_{rp}$  is the curvature of the preview path point, and  $\kappa_1$  and  $\kappa_2$  are the dimensionless proportionality coefficients.

**Remark 3.** The first term of (47) indicates that the control gain is adjusted by the curvature, which can avoid repeated overshoot of the steering angle on paths with a small curvature due to the excessive control gain. The second term of (47) implies that the adaptive adjustment strategy will consider the curvature and lateral error, and its purpose is to increase the path-tracking accuracy and be beneficial to the error convergence at large curvatures. If  $\kappa_1$  is given an appropriate value, the lateral error in the path with a small curvature will be within a small range. When the curvature exceeds 0.02, the lateral error term will intervene to resize the control gain. If  $\kappa_2$  is properly adjusted, the effect of the step signal caused by the switching condition is very slight. Because the steering gear of the AHMDT is generally a hydraulic actuator, it has a certain rise time to execute the switched step command, which can be verified by the continuous step test and U-shaped experiment, which will be introduced later.

## 6 Experimental results

The vehicle control algorithms are implemented in C++ under the Robot Operating System. The decision and planning layer is responsible for sending the desired trajectory information and decision signal to the vehicle control layer. The localization layer measures the real-time position and motion state of the vehicle, such as speed, acceleration, yaw angle, and yaw rate, using the integrated DGPS and IMU. The vehicle actuator and sensor layer can output the state of the actuator and load of the AHMDT through the CAN bus. Finally, all the information is received and applied by the vehicle control layer to conduct trajectory tracking control. The parameters of the trajectory tracking controllers are shown in Table 4.

### 6.1 Experiment of the longitudinal control

The first test is under the medium-speed and no-load working condition. The vehicle speed and desired speed comparison are shown in Figure 9(a). The speed error and road slope are shown in Figures 9(b) and (c), respectively. The maximum slope is 4.5% and  $-4.8\%$ , and the maximum uphill and downhill speed errors are 1 and 1.1 m/s, respectively. The speed errors of the remaining parts are all within 0.6 m/s. The DBFC is shown in Figure 9(d). The controller can compensate for the driving force, which is 90000 N at uphill conditions, to guarantee the accuracy of speed tracking.

**Table 4** Parameters of the vehicle and the controller for experiment

Parameter	Nominal value
Proportional coefficient $k_d/k_{p\alpha}/k_{pp}$	0.5/8/10
Integral coefficient $k_{i\alpha}(\tau_1, \tau_2)/k_{ip}(\tau_1, \tau_2)$	(3,1.5)/(2,3.5)
Dimensionless proportional coefficient $k_e$	$2 \times 10^{-6}$
Dead-zone bias $\vartheta$ (m/s)	0.6
Proportional coefficient $\kappa_1/\kappa_2$	12/0.15
Positive constant $a$	0.28
Damping factor $\zeta$	1.85
Sample time $\Delta t$ (s)	0.02

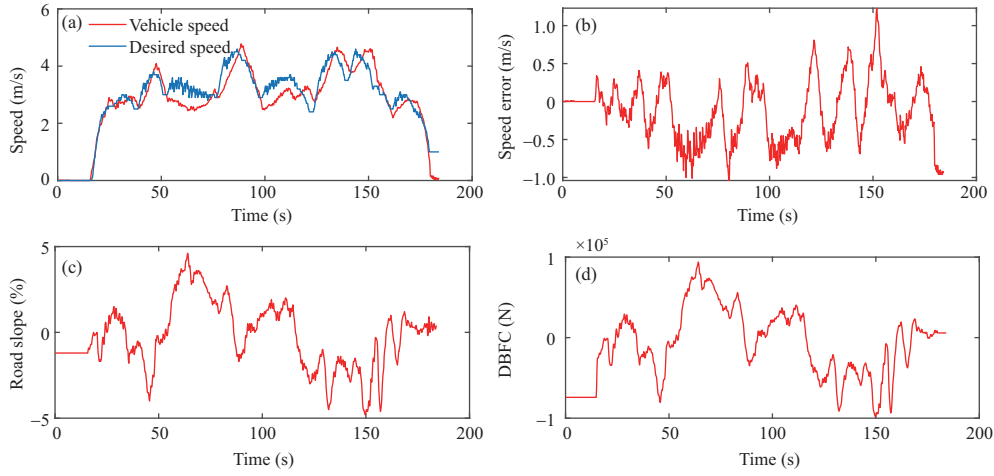


**Figure 9** (Color online) Test results of speed tracking control. (a) Speed; (b) speed error; (c) road slope; (d) DBFC.

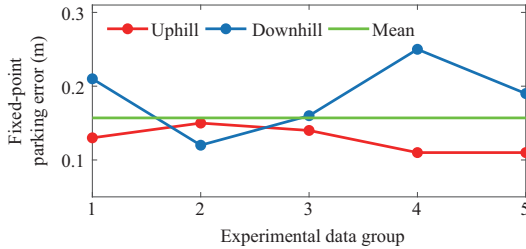


**Figure 10** (Color online) Fixed-point parking error.

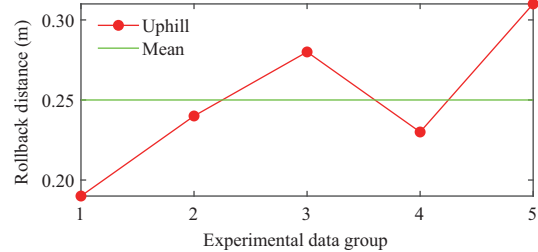


**Figure 11** (Color online) Rollback distance.

To test the fixed-point parking control and slope-start control, an AHMDT with a load of 200 tons was placed uphill and downhill on a 12% slope. The experimental results of the fixed-point parking control are shown in Figure 10. In the ten groups of experiments performed uphill and downhill, the maximum parking errors are 0.15 and 0.25 m, respectively, and the average parking error of the ten groups of experiments is 0.16 m, as shown by the green line. The evaluation index for the slope-start control is the rollback distance of the vehicle. Because it is impossible for the vehicle to roll back downhill, Figure 11 shows the five groups of uphill results. The maximum rollback distance is 0.31 m, and the average value is 0.25 m. The designed controller can improve the accuracy of fixed-point parking and reduce the rollback distance, which can provide a safety guarantee for the operation of AHMDTs on cliffs and ramps.

## 6.2 Experiment of the lateral control

The reference path and actual vehicle position under the U-shaped large-curvature condition are shown in Figure 12(a). The minimum radii of the curvature at the turning of two curves are 16.6 and 10.4 m, respectively. The actual speed during the path-tracking process is shown in Figure 12(b). The vehicle speeds in the straight section and corners are almost maintained at approximately 5.8 and 1.5 m/s. Figure 12(c) shows that the lateral error during path tracking in the straight section is within 0.2 m, and

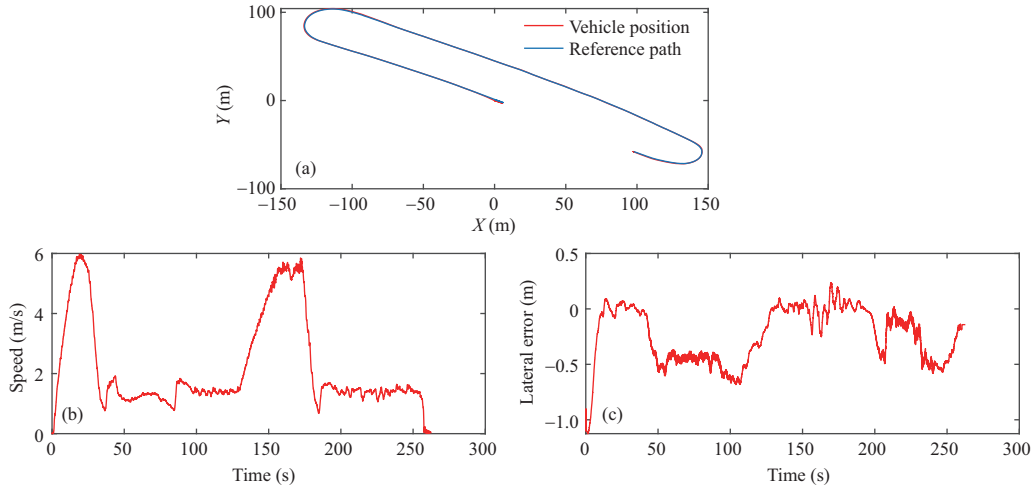


**Figure 12** (Color online) Test results of the U-shaped condition. (a) Trajectory comparison; (b) speed; (c) lateral error.

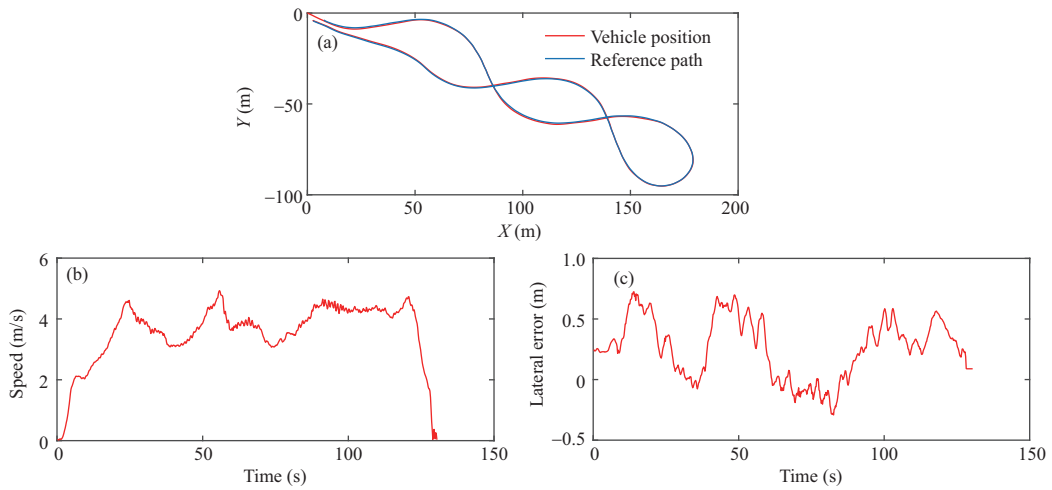


**Figure 13** (Color online) Test results of the 8-shaped condition. (a) Trajectory comparison; (b) speed; (c) lateral error.

the maximum lateral error is only 0.6 m under the turning conditions with large curvatures.

To increase the complexity of working conditions, the 8-shaped large-curvature condition was selected for testing. The reference path and actual vehicle position are shown in Figure 13(a). The minimum radius of the curvature at the turn of the path is 13.7 m. The actual speed during the path-tracking process is shown in Figure 13(b), and the speed is almost maintained at approximately 4.2 m/s during the test. Figure 13(c) shows that the maximum lateral error is up to 0.6 m during the continuous change of the path curvature due to the fast vehicle speed. However, the maximum lateral error under the turning conditions with large curvatures is  $-0.2$  m, and the negative sign means that the vehicle is driving on the inner circle of the path, which benefits from the preview distance calculated by the curvature and speed.

To verify the MRFC, the vertical parking condition commonly used by AHMDTs was selected. The condition often appears when an AHMDT loads and enters the parking lot. The reference path and actual position of the vehicle are shown in Figure 14(a). The minimum radius of the curvature at the turn of the path is 23.4 m. The actual speed and lateral error during the path-tracking process are shown in Figures 14(b) and (c), respectively. During the test, the vehicle speed was almost maintained at approximately 1.8 m/s. The vehicle was far away from the path when it started, and the MRFC algorithm made the lateral error quickly converge. Moreover, the maximum lateral error in the subsequent tracking process is approximately 0.3 m. The yaw angle error is shown in Figure 14(d). When the yaw angle error converged, it was kept at approximately  $2^\circ$ . When the vehicle finally parks in the given location, it can maintain an accurate position and attitude.

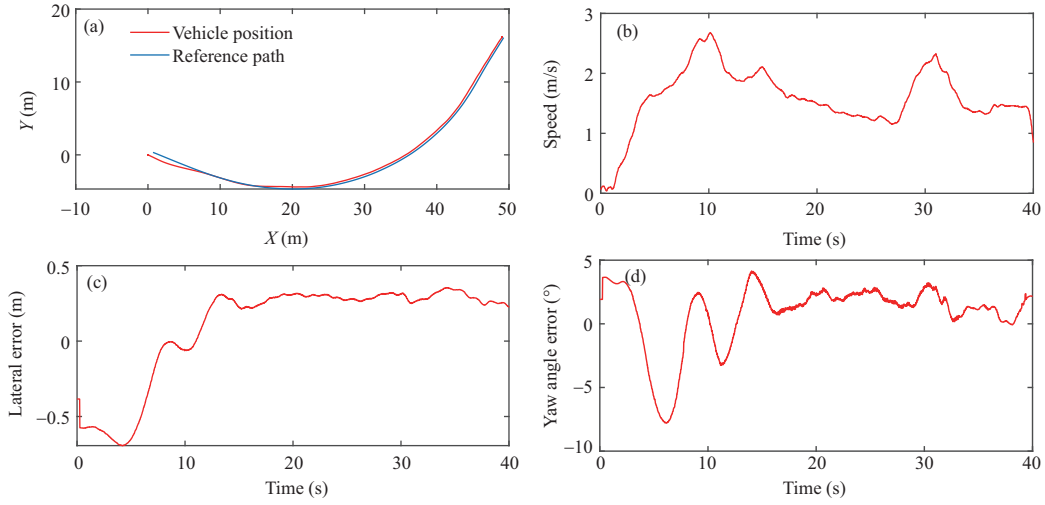


**Figure 14** (Color online) Results of the vertical parking test for the reversal scene. (a) Trajectory comparison; (b) speed; (c) lateral error; (d) Yaw angle error.

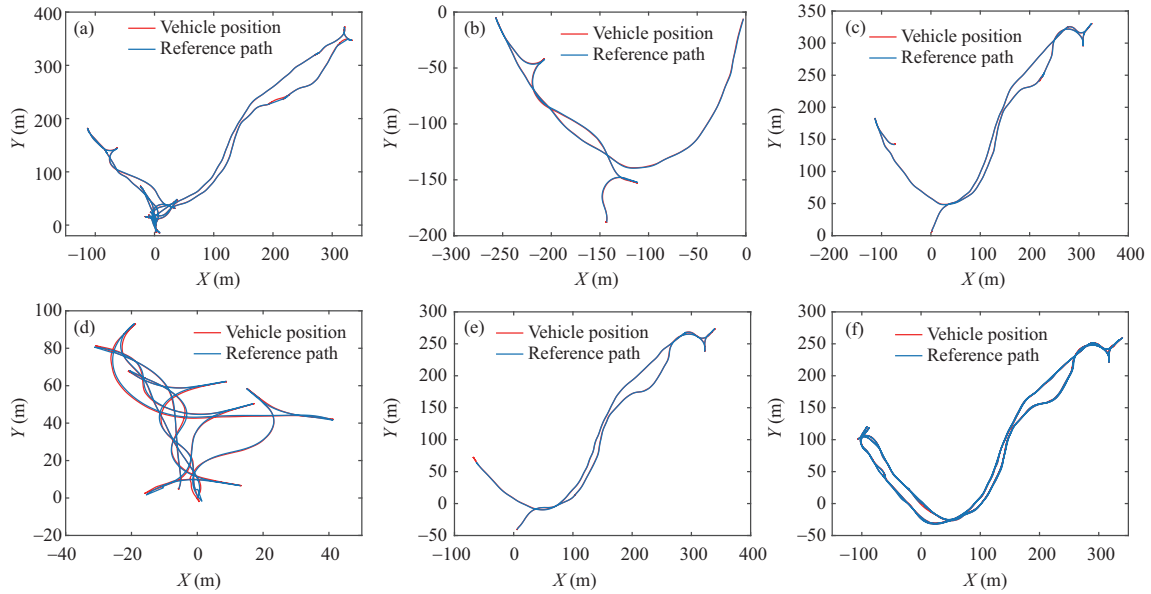


**Figure 15** (Color online) Results of the end-to-end autonomous mining operations.

**Table 5** Data analysis of the end-to-end autonomous mining operation experiments

Error	Mean	Standard deviation
Lateral error (forward)	0.271 (m)	0.064 (m)
Lateral error (reverse)	0.256 (m)	0.083 (m)
Yaw angle error (reverse)	2.7 (°)	0.672 (°)
Speed error	0.87 (km/h)	0.245 (km/h)

### 6.3 Experiment of the end-to-end autonomous mining operations

To make the experiment more convictive, the Monte Carlo method was applied to prove the effectiveness of the proposed trajectory tracking control method by analyzing six groups of end-to-end autonomous mining operation experimental data. The reference path and actual vehicle position are shown in Figure 15. The scene contains tasks that AHMDTs usually need to perform, such as loading, transportation, and unloading.

Six groups of experimental data in an end-to-end autonomous mining operation process were analyzed using the standard deviation and mean value, as shown in Table 5. The mean values of the lateral error

are 0.271 and 0.256 m for the forward condition and reverse condition, respectively. The mean and standard deviation values of the yaw angle error are  $2.27^\circ$  and  $0.672^\circ$ , respectively. The presented MRFC not only leads to a small lateral error but also guarantees that the vehicle follows the desired yaw angle of the reference path. The mean and standard deviation values of the speed error are 0.87 and 0.245 km/h, which indicates that integrating the DBFC and SFC can guarantee accurate longitudinal control only with a set of SFC parameters in different load and slope conditions. The results obtained by the Monte Carlo method prove the effectiveness and practicability of the proposed trajectory tracking control method from another aspect.

## 7 Conclusion

This paper presents a trajectory tracking control method for AHMDTs in open-pit mining. The proposed method was successfully applied to AHMDTs, which can realize accurate lateral control and longitudinal control and support the operation of loading, unloading, and transportation tasks in open-pit mines. An algorithm that integrates the DBFC and SFC was designed to guarantee accurate longitudinal control only with a set of SFC control parameters. Moreover, an MRFC method is proposed to deal with reverse-path tracking, which can simultaneously reduce lateral and yaw angle errors. In addition, a modified Stanley controller considering collaborative preview based on speed and curvature was constructed to achieve accurate path-tracking control when the vehicle is in forward gear. Experimental results show that the proposed lateral and longitudinal control method can achieve trajectory tracking with reasonable accuracy, which has high engineering application value. In continuous operation experiments, many functions, such as loading, transporting, unloading, and cooperation with a shovel, have been fully tested.

**Acknowledgements** This work was supported by National Key R&D Program of China (Grant No. 2021YFB2501803), National Natural Science Foundation of China (Grant Nos. 52222216, 52102394, U20A2225, U2013601), Anhui Province Natural Science Funds for Distinguished Young Scholar (Grant No. 2308085J02), Scientific and Technological Innovation 2030 — “New Generation Artificial Intelligence” Major Project (Grant No. 2022ZD0116305), and CAAI-Huawei MindSpore Open Fund. Finally, Liang CHEN and Yu DONG became a legal couple on the last working day of 2022. Liang CHEN wants to thank, in particular, the patience, support and love from Yu DONG over the past six years.

## References

- Li J, Zhan K. Intelligent mining technology for an underground metal mine based on unmanned equipment. *Engineering*, 2018, 4: 381–391
- Berglund T, Brodnik A, Jonsson H, et al. Planning smooth and obstacle-avoiding B-spline paths for autonomous mining vehicles. *IEEE Trans Automat Sci Eng*, 2009, 7: 167–172
- de Vries J, de Koster R, Rijdsdijk S, et al. Determinants of safe and productive truck driving: Empirical evidence from long-haul cargo transport. *Transportation Res Part E-Logistics Transportation Rev*, 2017, 97: 113–131
- Zhao Z, Bi L. A new challenge: path planning for autonomous truck of open-pit mines in the last transport section. *Appl Sci*, 2020, 10: 6622
- Kansake B A, Frimpong S. Analytical modelling of dump truck tire dynamic response to haul road surface excitations. *Int J Min Reclamation Environ*, 2020, 34: 1–18
- Mendes J B, D'Angelo M F S V, Maia N A, et al. A hybrid multiobjective evolutionary algorithm for truck dispatching in open-pit-mining. *IEEE Latin Am Trans*, 2016, 14: 1329–1334
- Gao Y, Ai Y, Tian B, et al. Parallel end-to-end autonomous mining: an IoT-oriented approach. *IEEE Internet Things J*, 2019, 7: 1011–1023
- Volvo Tests a Self-Driving Truck in a Swedish Mine, Blows Our Minds. Accessed: Dec. 17, 2018. <https://www.guidingtech.com/61345/volvo-tests-self-driving-truck-swedish-mine/>
- Ding J L, Liu T, Zhao Y, et al. HAPNet: a head-aware pedestrian detection network associated with the affinity field. *Sci China Inf Sci*, 2022, 65: 160102
- Chen Y, Huang S, Fitch R. Active SLAM for mobile robots with area coverage and obstacle avoidance. *IEEE ASME Trans Mechatron*, 2020, 25: 1182–1192
- Qin Z, Chen X, Hu M, et al. A novel path planning methodology for automated valet parking based on directional graph search and geometry curve. *Robotics Autonom Syst*, 2020, 132: 103606
- Xue Z B, Liu J C, Wu Z X, et al. Development and path planning of a novel unmanned surface vehicle system and its application to exploitation of Qarhan Salt Lake. *Sci China Inf Sci*, 2019, 62: 084202
- Qin Z, Chen L, Hu M, et al. A lateral and longitudinal dynamics control framework of autonomous vehicles based on multi-parameter joint estimation. *IEEE Trans Veh Technol*, 2022, 71: 5837–5852
- Wang Y L, Zheng H Y, Zong C F, et al. Path-following control of autonomous ground vehicles using triple-step model predictive control. *Sci China Inf Sci*, 2020, 63: 209203
- Chen L, Qin Z, Hu M et al. Path tracking controller design of automated parking systems via NMPC with an instructible solution. *Research Square*, 2022, doi: 10.21203/rs.3.rs-1388380/v1
- Ni J, Hu J, Xiang C. Robust path following control at driving/handling limits of an autonomous electric racecar. *IEEE Trans Veh Technol*, 2019, 68: 5518–5526
- Brown M, Funke J, Erlien S, et al. Safe driving envelopes for path tracking in autonomous vehicles. *Control Eng Pract*, 2017, 61: 307–316

- 18 Wallace R S, Stentz A, Thorpe C E, et al. First results in robot road-following. In: Proceedings of the 9th International Joint Conference on Artificial Intelligence, 1985. 1089–1095
- 19 Thrun S, Montemerlo M, Dahlkamp H, et al. Stanley: the robot that won the DARPA grand challenge. *J Field Robotics*, 2006, 23: 661–692
- 20 Rokonzaman M, Mohajer N, Nahavandi S, et al. Review and performance evaluation of path tracking controllers of autonomous vehicles. *IET Intell Trans Sys*, 2021, 15: 646–670
- 21 Zheng H, Wu J, Pan K, et al. Research on control target of truck platoon based on maximizing fuel saving rate. *SAE Int J Veh Dyn Stab NVH*, 2020, 4: 135–150
- 22 Negash N M, Yang J. Anticipation-based autonomous platoon control strategy with minimum parameter learning adaptive radial basis function neural network sliding mode control. *SAE Int J Veh Dyn Stab NVH*, 2022, 6: 247–265
- 23 Leonard J, Barrett D, How J, et al. Team MIT Urban Challenge Technical Report. MIT-CSAIL-TR-2007-058. 2007
- 24 Shakouri P, Ordys A, Laila D S, et al. Adaptive cruise control system: comparing gain-scheduling PI and LQ controllers. *IFAC Proc Volumes*, 2011, 44: 12964–12969
- 25 Gerdes J C, Hedrick J K. Vehicle speed and spacing control via coordinated throttle and brake actuation. *Control Eng Pract*, 1997, 5: 1607–1614
- 26 Qin Z, Chen L, Fan J, et al. An improved real-time slip model identification method for autonomous tracked vehicles using forward trajectory prediction compensation. *IEEE Trans Instrum Meas*, 2021, 70: 1–12
- 27 Ang J, Bagh S, Ingalls B P, et al. Considerations for using integral feedback control to construct a perfectly adapting synthetic gene network. *J Theor Biol*, 2010, 266: 723–738
- 28 Samson C. Time-varying feedback stabilization of car-like wheeled mobile robots. *Int J Robotics Res*, 1993, 12: 55–64